Structural additive manufacturing parts bio-inspired from trabecular bone form-function relationship

Nicolas Cadoret, Julien Chaves-Jacob, Jean-Marc Linares

Materials & Design 231 (2023) 112029

Contents lists available at ScienceDirect

Materials & Design

journal homepage: www.elsevier.com/locate/matdes

Structural additive manufacturing parts bio-inspired from trabecular bone form-function relationship

Nicolas Cadoret, Julien Chaves-Jacob *, Jean-Marc Linares

Aix Marseille Université, CNRS, ISM, Inst Mouvement Sci, UMR 7287, Marseille, France

HIGHLIGHTS

- The trabecular form-function relationship was condensed into 2 equations, linking volume fraction and Fabric Tensor to local stress.
- A bio-inspired porous pattern was proposed to reproduce the trabecular form-function relationship by adapting its geometry to stress.
- A mass reduction method was established in which a mechanical part architecture is locally adapted to the stress gradient.
- At equal mass, the proposed 3D mass reduction method showcases twice the bending stiffness when compared to topology optimization.

GRAPHICAL ABSTRACT

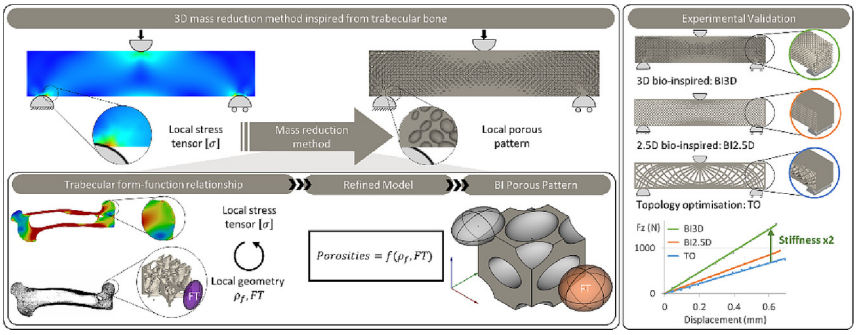

ARTICLE INFO

Article history:
Received 29 March 2023
Revised 15 May 2023
Accepted 20 May 2023
Available online 25 May 2023

Keywords:
Mass reduction method
Bio-inspiration
Trabecular bone
Fabric Tensor
Volume Fraction

ABSTRACT

Mass reduction and strength-to-weight optimisation are of increasing interest in mechanical engineering. Natural materials such as bone face the same challenges and strike an optimal balance between weight and mechanical performance. Several approaches sought to reproduce trabecular bone's mechanical efficiency, for example topology optimisation or cellular materials. These approaches are often restricted by their computational cost or their spatial homogeneity. Here we develop a 3D mass reduction method bio-inspired from trabecular bone that provides both fast computation and stress driven architecture. The mass reduction method is based on a bio-inspired porous pattern. The pattern is locally adapted to the estimated stress in a mechanical part through an algorithm. This results in an optimised porous architecture that mimics the trabecular form-function relationship. This 3D mass reduction method was validated through 3-point bending experiments. At equal mass, the proposed method showed 66 % improvement in bending stiffness compared to a 2.5D bio-inspired method and 111 % improvement compared to a topology optimisation method. Our results demonstrate the potential of the proposed method for strength-to-weight optimisation. It is applicable in various industries to lighten parts, reduce raw material usage, design composite sandwich cores or personalised bone-tissue scaffolds.

1. Introduction

The environmental impact of human activities has been a concern of the scientific community for several decades, especially

* Corresponding author.
E-mail address: julien.chaves-jacob@univ-amu.fr (J. Chaves-Jacob).

https://doi.org/10.1016/j.matdes.2023.112029
0264-1275/

with recent events highlighting this impact [1]. In mechanical engineering, there are three ways to reduce environmental impact: reduce the amount of raw materials used, reduce the complexity of assemblies and the number of parts, and reduce the weight of parts. Recently, these 3 aspects have become more practical thanks to advances in additive manufacturing (AM) in industrial sectors [2,3]. For example, in aerospace, AM can reduce materials' buy-to-fly ratio from 20:1 to 3:1. AM techniques were used to manufacture the Ariane 6 rocket injector which achieved to consolidate 248 individual components as a single component. AM has also helped divide the weight of some A320 parts by a factor of 2 [4].

With regards to mass reduction, since there's often little room for performance loss in demanding industrial sectors, this means increasing mechanical parts' strength-to-weight ratio [5]. This is possible by selecting high-performance materials such as titanium, technical ceramics or composites [6]. Unfortunately, these materials increase costs and can sometimes be hard to recycle. Other high-performance materials exist in nature, often with high strength-to-weight ratios in the same order of magnitude as composites and technical ceramics [7,8]. However, natural materials are mostly made of polymers or ceramics which by themselves showcase low mechanical performance [9,10]. It appears most of their strength comes from their microstructure and hierarchical nature rather than their chemical composition [9–12]. In fact, micromechanical models have been successfully applied to study microstructural effects on the macroscopic behavior of trabecular architecture [13] and to investigate vertebral trabecular bone static and dynamic behavior [14].

Bone is one of the best documented examples of optimised natural material. Bones fulfil key mechanical functions in endoskeletons. They are anchor points for muscles, provide a frame which keeps the body upright and are involved in body segments' movement [15]. Inside bones, the porous, orthotropic, asymmetric and heterogenous trabecular architecture transfers mechanical loads to the fully dense cortical bone [16]. As a living tissue, trabecular bone also adapts to the mechanical stress it undergoes [17,18]. Therefore, the trabecular architecture is relevant for the development of high-performance material architectures.

In the literature, the trabecular architecture has been imitated in numerous ways. On one hand, numerical methods such as topology optimisation [19–21], remodeling-based approaches [22–24] and micromechanical approaches [25,26] have shown promising results. However, these methods require significant computational resources to achieve an architecture as detailed as trabecular bone. On the other hand, cellular materials have also been studied in detail [27].

Cellular materials typically consist of a periodic repetition of identical cellular units. The simplest units, strut-based lattices, showcase geometrical discontinuities at joints which results in harmful stress concentrations Slender struts also tend to buckle if their aspect ratio is insufficient. These stress concentrations can be addressed by introducing fillets at joints [28]. Stress concentration were also compensated using bi-material lattices with tailored compressive stress–strain response [29]. To reduce the periodicity of strut-based lattices, random Voronoï lattices have been proposed [30–34]. Moreover, to balance the aforementioned problems of strut-based lattices, *iso*-surface strut-based lattices have been developed based on Triply Periodic Minimal Surfaces (TPMS) [35]. TPMS are cellular materials whose unit cells are based on continuous mathematical surfaces. This helps reduce the risks of stress concentrations and strut buckling [36–38]. These cellular materials tend to be spatially homogeneous and gradient structures whose geometric properties vary as a function of mechanical stress have also been proposed [39,40]. Deep learning and machine learning models have respectively been used to tune the mechanical response of stochastic and spinodoid gradient structures [41,42]. However, these models require large datasets of natural architectures to be properly trained.

Therefore, as the range of approaches shows, reproducing the complexity of the trabecular architecture is not easy. Indeed, trabecular bone is a composite, hierarchical, self-healing cellular material. Reproducing all of these properties in an engineering context will not be easily achievable. When faced with such a challenge in bio-inspiration, the ISO 18458 standard recommends abstraction: drawing general conclusions based on observations of the biological object [43]. A deep understanding of the biological object is used to identify its most significant properties. These properties are then transferred to the technological object by analogy.

With regard to trabecular architecture, there are several significant properties. First, bone adapts to the mechanical stress it undergoes. As a result of this functional adaptation, the trabecular architecture is oriented along lines of principal stress [44–46]. Secondly, between species of different size, there's an allometric scaling of the trabecular pattern [47]. Third, because of the heterogeneous nature of trabecular bone, its mechanical properties will vary between species, bones, anatomic sites, etc. It has been shown that this variation is mostly correlated to the local volume fraction (ρ_f) and Fabric Tensor (FT) [48,49]. Hence, the link between mechanical stress, ρ_f and FT. could be an expression of the trabecular form-function relationship. Previously, 2.5D mass reduction methods bio-inspired from the trabecular form-function relationship [50,51] have been developed and showed higher stiffness at equal mass when compared to topology optimization.

Here, a 3D mass reduction method bio-inspired from the trabecular form-function relationship is developed. First, in section 2, the trabecular form-function relationship's equations are presented. Then, in section 3, a bio-inspired porous pattern is established with a mathematical model linking pattern parameters, FT and ρ_f. In section 4, a bio-inspired mass reduction algorithm is developed based on the aforementioned bio-inspired porous pattern. This algorithm reproduces the established trabecular form-function relationship in a mechanical part. Finally, in section 5, an experiment is proposed to quantify the performance of the mass reduction method through 3-point bending experiments.

2. Trabecular form-function relationship

As mentioned above, it has been shown that the variability in mechanical properties of trabecular bone is mostly correlated with its architecture. References from the literature show that trabecular architectures are best described by their volume fraction and fabric tensor. In fact, several authors have proposed equations that link both measures to mechanical stress, quantified through the Von Mises stress σ_{VM}. These equations are presented in details here.

2.1 vol. fraction

The volume fraction (ρ_f) or apparent density of a cellular material is defined as the density of the cellular solid divided by that of the solid it is made from. For trabecular bone, it is also measured as the bone volume (BV) in a given sample over the total volume of that sample (TV), *eq.(1)*.

Several works have established a mathematical link between ρ_f and the estimated state of stress in a given bone. For example, Audibert *et al.* estimated the stress in the human femur during walking to link the volume fraction gradient and Von Mises stress using *eq.(1)* [50].

$$\rho_f = \frac{BV}{TV} = 3.07\,(\sigma_{VM}/R_e)^{0.59} \quad (1)$$

With $\sigma_{VM} = \sqrt{\frac{1}{2}\left[(\sigma_1-\sigma_2)^2+(\sigma_2-\sigma_3)^2+(\sigma_3-\sigma_1)^2\right]}$, the Von Mises stress and R_e the elastic limit of bone.

The Von Mises stress criterion was used in this article to reflect the work presented in Audibert *et al.* It is widely used in an engineering context and is easily available through most finite element solver. It is also widely used in the biomechanical literature as an estimation of local stress in bones.

2.2. Fabric Tensor

The FT is defined as a symmetric second rank tensor which characterizes the arrangement of the microstructural components in a multiphase or porous material [52]. For trabecular samples, the FT is based on the equation of the ellipsoid best-fitted to the Mean Intercept Length (MIL) point cloud, which represents the mean length of material in all directions [53,54]. This FT (**M**) quantifies the trabecular anisotropy through the ellipsoid's orientation and shape, described by the radii M_1, M_2, M_3 (**M**'s eigenvalues).

Indeed, trabecular tissue that regularly undergoes significant anisotropic stress will adapt to it and showcase an oriented architecture. Most bone tissue will be oriented along the principal stress' directions [44–46] and the FT will be prolate in the same direction. On the other hand, trabecular tissue subjected to isotropic stress will be less heavily oriented with an FT closer to a sphere.

In this article, the shape of the FT ellipsoid is described through two ratios Y_1 and Y_2 between radii M_1, M_2, M_3, eq.(2).

$$\begin{cases} Y_1 = M_1/M_3 \geq 1 \\ Y_2 = M_1/M_2 \geq 1 \end{cases} \quad (2)$$

With $M_1 \geq M_2 \geq M_3$

For example:

- if both ratios Y_1 and Y_2 are close to 1, the FT ellipsoid will be of spherical shape,
- if Y_1 and Y_2 are high the ellipsoid will be prolate,
- if Y_1 is high and Y_2 is close to 1 the ellipsoid will be oblate.

Two examples comparing trabecular samples' 3D architectures and their MIL-based FT are shown in Fig. 1. These two samples were taken from Doube *et al*'s dataset [55] and analysed through BoneJ2′s anisotropy function [56]. Both samples come from femoral condyles; the first from an Afghan pika (Fig. 1(a)) and the second from an Asian elephant (Fig. 1(b)). MIL-based FT ellipsoids were represented and color-coded based on their first shape ratio Y_1. The more anisotropic sample (a) presents a heavily oriented architecture and a prolate FT ellipsoid. The quasi-isotropic sample (b) shows an FT ellipsoid whose shape is closer to a sphere.

Hence, **M** is a representation of the local trabecular architecture. As a consequence of the trabecular form-function relationship, a mathematical link between **M** and the estimated local mechanical stress should exist. Such a relationship has already been proposed [57]. Hazrati Marangalou *et al.* estimated the state of stress in the human femur during typical physical activity using finite element analysis. Based on this estimation, they estimated FT throughout the bone. They then compared these estimated values with some measured from CT scans of several human femurs. Using likelihood ratio tests, the authors showed less than 10 % of averaged norm differences between estimated and measured FT. Similar results were reproduced for the trotting horse humerus, demonstrating the validity of the relationship in various animal models [58]. The equation used here is adapted from [57] based on the hypothesis that compressive and tensile stresses have the same effect on trabecular architecture [49].

Let $\sigma_1, \sigma_2, \sigma_3$ be the principal stresses. M_i is the FT radius following the same direction as σ_i. $\sigma_1, \sigma_2, \sigma_3$ are oriented along vectors $\mathbf{u}, \mathbf{v}, \mathbf{w}$ respectively, which will be used later in this work.

$$M_i = \frac{|\sigma_i|^{1/4}}{\left(|\sigma_1|^{1/4}\,|\sigma_2|^{1/4}\,|\sigma_3|^{1/4}\right)^{1/3}} \quad (3)$$

With $|\sigma_1| \geq |\sigma_2| \geq |\sigma_3|$.

3. Mimicking trabecular form-function relationship in a bio-inspired porous pattern

Hence, the trabecular form-function relationship can be expressed through, ρ_f, FT and their link to the estimated mechanical stress, *eqs.(1) and (3)*. We hypothesise that it is possible to mimic trabecular architecture's optimisation by reproducing its form-function relationship in a bio-inspired porous pattern. Here, the parametric pattern developed for that purpose is first presented. A mathematical model which links pattern parameters, ρ_f and FT is then developed.

3.1. Bio-inspired porous pattern and parameters

To ensure that low volume fraction can be achieved, a pattern with dense packing of porosities was used. Based on crystallographic theory, the face-centred cubic (FCC) pattern was selected as it allows the densest packing of nodes in a given volume. The length of the cube's side is controlled through the pattern size *p*. Then, at each node in the FCC pattern, porosities of ellipsoidal

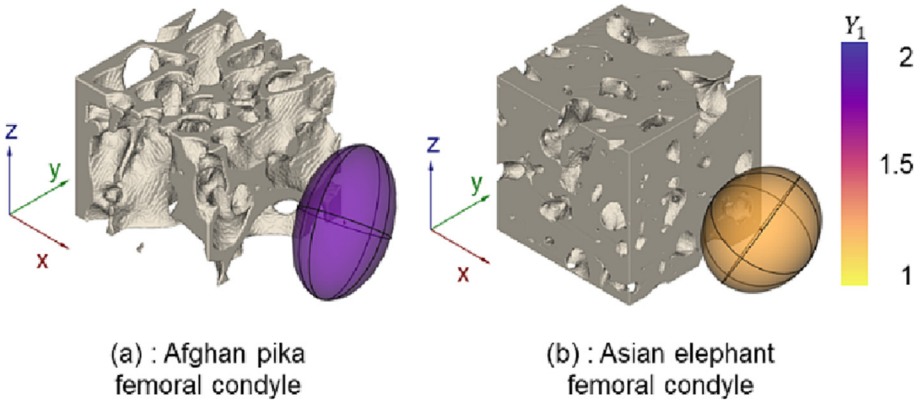

Fig. 1. Fabric Tensor from two bone samples from different species, presenting varying degrees of anisotropy, samples dimensions are 1.29 mm × 1.29 mm × 1.15 mm (a) and 4.02 mm × 4.02 mm × 4.02 mm (b) (dataset: [55]).

shapes were created. The ellipsoid shape was chosen because it ensured C2 continuity within the porosity and reproduced the shape of the MIL-based FT. Porosities' size, shape and orientation are respectively controlled through the size of the ellipsoid's principal semi-axes ($a \leq b \leq c$), the ratios between principal semi-axes (c/a and c/b) and the ellipsoid's axis of rotation (angle θ around an axis **e**). In practice, this bio-inspired porous pattern was implemented using FreeCAD parametric modelling [59] as shown in Fig. 2(a). Porosity parameters are detailed in Fig. 2(b).

In order to compute ρ_f in the bio-inspired porous pattern, crystallographic theory is used. There is the equivalent volume of 4 ellipsoid porosities in a bio-inspired porous FCC pattern. As such, ρ_f in a pattern of size p with porosities dimensions a, b and c, can be obtained through eq.(4).

$$\rho_f = \frac{V_{cube} - 4\,V_{ellipsoid}}{V_{cube}} = 1 - \frac{4\left(\frac{4}{3}\,\pi\,a\,b\,c\right)}{p^3} \tag{4}$$

As seen in section 2.2, FT characterises the degree of anisotropy and orientation of any porous material. Thus, it is possible to measure an FT for the proposed bio-inspired porous pattern. An example is shown on Fig. 3(a) using a bio-inspired porous pattern that was analysed using BoneJ2′s anisotropy plugin. Measured FT ellipsoid and its dimensions are detailed on Fig. 3(b). As expected:

- FT orientation follows porosity orientation (θ, **e**);
- FT size depends on p and ρ_f;
- FT shape ratios Y_1 and Y_2 depend on porosity shape ratios c/a and c/b.

3.2. Mathematical model between bio-inspired porous pattern parameters and resulting Fabric Tensor

The aim of this section is to establish a mathematical model between pattern parameters, as defined in section 3.1., and resulting FT and volume fraction in the pattern. Subsequently, this model will be used in the 3D mass reduction method (section 4) to calculate a set of parameters that produces a target FT and volume fraction. These target values can be calculated to mimic the trabecular form-function relationship, defined in section 2.

3.2.1. Tested parameters

First, RS factors (x_i) were selected: porosity shape ratios ($x_1 = c/a$, $x_2 = c/b$) and volume fraction ($x_3 = \rho_f$). Variation ranges $[MIN(x_i); MAX(x_i)]$ were defined for each factor, as detailed in Table 1. The variation ranges for porosity shape ratios were selected to cover the widest range of possible architectures whilst maintaining consistency with values observed in different trabecular samples described in the literature [24,60]. Centred-normalised variables (X_1, X_2, X_3), between parenthesis in Table 1, were calculated using eq.(5). Two responses were studied: one for each FT shape ratio ($Y_1 = M_1/M_3$ and $Y_2 = M_1/M_2$) as detailed in Table 2.

$$X_i = \frac{2[x_i - MEAN(x_i)]}{MAX(x_i) - MIN(x_i)} \tag{5}$$

Then, following a Design Of Experiment methodology, a set of 15 experiments were generated with the help of Nemrodw software [61,62], describing a cubic experimental domain. Accordingly, 15 bio-inspired porous patterns were generated, voxelised and analysed using BoneJ2′s anisotropy plugin to determine FT components (M_1, M_2, M_3) and response values (Y_1, Y_2). Table 3 gives an overview of the experimental setup, variable values and measured responses.

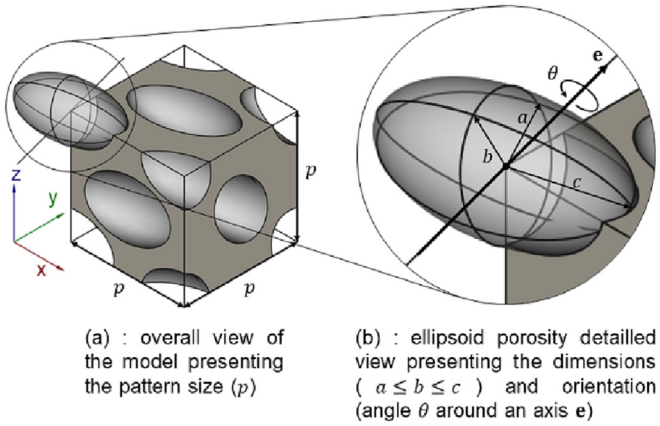

(a) : overall view of the model presenting the pattern size (p)

(b) : ellipsoid porosity detailled view presenting the dimensions ($a \leq b \leq c$) and orientation (angle θ around an axis **e**)

Fig. 2. Bio-inspired porous pattern model presenting the different parameters.

3.2.2. Generic model

Afterward, a generic mathematical model (GM) was fitted to the results in Table 3 in order to link Y_1 and Y_2 to X_1, X_2 and X_3 using second order polynomials *eqs.(6) and (7)*. Polynomial coefficients were estimated using the pseudo-inverse Method [63].

$$\begin{aligned} Y_{1_{GM}}(n) &= a_{0_{GM}} + a_{1_{GM}}X_1(n) + a_{2_{GM}}X_2(n) + a_{3_{GM}}X_3(n) \\ &+ a_{11_{GM}}X_1^2(n) + a_{22_{GM}}X_2^2(n) + a_{33_{GM}}X_3^2(n) \\ &+ a_{12_{GM}}X_1(n)X_2(n) + a_{13_{GM}}X_1(n)X_3(n) + a_{23_{GM}}X_2(n)X_3(n) \end{aligned} \tag{6}$$

$$\begin{aligned} Y_{2_{GM}}(n) &= b_{0_{GM}} + b_{1_{GM}}X_1(n) + b_{2_{GM}}X_2(n) + b_{3_{GM}}X_3(n) \\ &+ b_{11_{GM}}X_1^2(n) + b_{22_{GM}}X_2^2(n) + b_{33_{GM}}X_3^2(n) \\ &+ b_{12_{GM}}X_1(n)X_2(n) + b_{13_{GM}}X_1(n)X_3(n) + b_{23_{GM}}X_2(n)X_3(n) \end{aligned} \tag{7}$$

With $X_i(n)$ the variable values for a given experiment n, a_{iGM}, $b_{i_{GM}}$ the model coefficients for $Y_{1_{GM}}$ and $Y_{2_{GM}}$ respectively. This first mathematical model, called the Generic Model (GM), can be refined to further improve accuracy.

3.2.3. Refined model

In order to refine GM, non-significant variables must be removed. To do so, predicted responses were estimated which differ from measured responses. The difference for each experiment n can be quantified using residues $R_1(n)$ and $R_2(n)$ in *eq.(8)*.

$$\begin{cases} R_1(n) = Y_1(n) - Y_{1_{GM}}(n) \\ R_2(n) = Y_2(n) - Y_{2_{GM}}(n) \end{cases} \tag{8}$$

Based on these residues, Standard Deviations $SD(Y_1)$, $SD(Y_2)$ can be computed using *eq.(9)*.

$$SD(Y_i) = \sqrt{\frac{1}{N_e - N_f}\sum_{n=1}^{N_e} R_i(n)^2} \tag{9}$$

With N_e the number of experiments, N_f the number of coefficients in the equations (which will decrease during decimation). The following process was followed to obtain the Refined Model (RM):

- Coefficients a_{iGM}, $b_{i_{GM}}$ were removed one after the other in inverse order of influence, suppressing the the associated variable.
- Coefficients were re-estimated using the pseudo-inverse method.
- Residues ($R_1(n)$, $R_2(n)$) and standard deviations ($SD(Y_1)$, $SD(Y_2)$) were re-calculated.

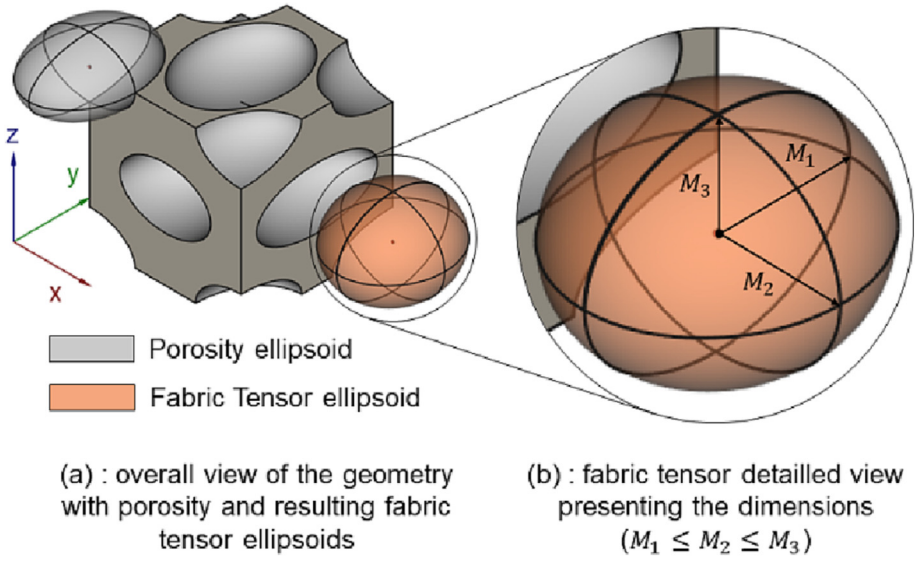

Fig. 3. Comparison between bio-inspired porous pattern geometry and resulting Fabric Tensor.

Table 1
Model factors and value ranges, corresponding centred-normalised variables are written in parenthesis.

Factor		Definition	MIN	MEAN	MAX
$\frac{c}{a}$	(X_1)	1st porosity shape ratio	1.00 (-1)	1.50 (0)	2.00 (1)
$\frac{c}{b}$	(X_2)	2nd porosity shape ratio	1.00 (-1)	1.50 (0)	2.00 (1)
ρ_f	(X_3)	Volume fraction	0.20 (-1)	0.55 (0)	0.90 (1)

Table 2
Model responses.

Response		Definition
$\frac{M_1}{M_3}$	(Y_1)	1st Fabric Tensor shape ratio
$\frac{M_1}{M_2}$	(Y_2)	2nd Fabric Tensor shape ratio

$SD(Y_1)$ and $SD(Y_2)$ were mapped throughout the refining process to study the evolution of accuracy, as shown on Fig. 4. Removed parameters at every decimation step are given on the x-axis.

Standard deviations are stable at first but removing parameters a_{13} and b_{23} produces a break in the standard deviation curves. Further steps significantly increase standard deviations. The refining process was stopped before that step, parameters a_1, a_3 and a_{13}; b_2, b_3 and b_{23} were kept resulting in the Refined Model (RM) *eqs. (10) and (11)*.

Table 4 *and* Table 5 give GM and RM coefficients for Y_1 and Y_2 respectively.

$$Y_{1_{RM}} = a_{0_{RM}} + a_{1_{RM}} X_1 + a_{3_{RM}} X_3 + a_{13_{RM}} X_1 X_3 \tag{10}$$

$$Y_{2_{RM}} = b_{0_{RM}} + b_{2_{RM}} X_2 + b_{3_{RM}} X_3 + b_{23_{RM}} X_2 X_3 \tag{11}$$

To illustrate that no significant errors are committed because of the refining process, RS were mapped for $(Y_{1_{GM}}, Y_{2_{GM}}, Y_{1_{RM}}, Y_{2_{RM}})$ as presented in Fig. 5 *and* Fig. 6. 4D space is necessary to represent all 3 variables (X_1, X_2, X_3) along with predicted responses. To achieve this, variables are mapped along each axis in 3D space. At different

Table 3
Set of experiments (X_i values generated by Nemrodw) and corresponding measured responses.

Experiment number (n)	$\frac{c}{a}(X_1)$	$\frac{c}{b}(X_2)$	$\rho_f(X_3)$	Y_1	Y_2
1	1 (-1)	1 (-1)	0.2 (-1)	1.003	1.001
2	2 (1)	1 (-1)	0.2 (-1)	2.032	1.019
3	1 (-1)	2 (1)	0.2 (-1)	1.009	1.994
4	2 (1)	2 (1)	0.2 (-1)	1.562	1.554
5	1 (-1)	1 (-1)	0.9 (1)	1.015	1.010
6	2 (1)	1 (-1)	0.9 (1)	1.165	1.016
7	1 (-1)	2 (1)	0.9 (1)	1.008	1.175
8	2 (1)	2 (1)	0.9 (1)	1.127	1.119
9	1 (-1)	1.5 (0)	0.55 (0)	1.009	1.187
10	2 (1)	1.5 (0)	0.55 (0)	1.302	1.147
11	1.5 (0)	1 (-1)	0.55 (0)	1.182	1.012
12	1.5 (0)	2 (1)	0.55 (0)	1.144	1.298
13	1.5 (0)	1.5 (0)	0.2 (-1)	1.148	1.146
14	1.5 (0)	1.5 (0)	0.9 (1)	1.084	1.072
15	1.5 (0)	1.5 (0)	0.55 (0)	1.154	1.152

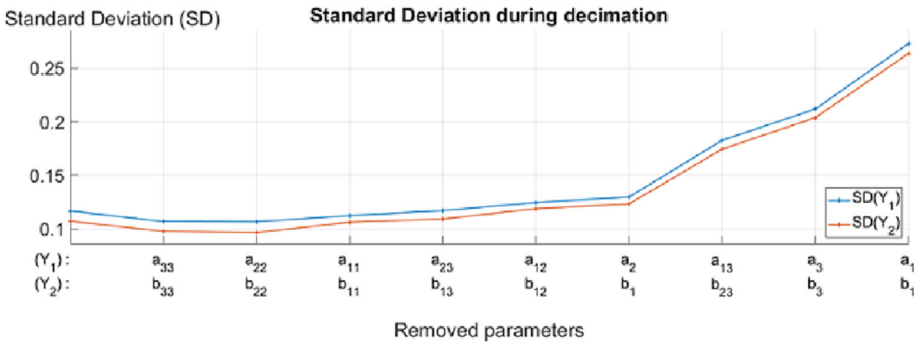

Fig. 4. Standard Deviation evolution during parameter decimation to obtain the refined model.

Table 4
Y_1 coefficients before and after parameter decimation.

Coefficients	Generic Model	Refined Model
a_0	1.114	1.196
a_1	0.214	0.214
a_2	−0.055	
a_3	−0.135	−0.135
a_{11}	0.052	
a_{22}	0.059	
a_{33}	0.012	
a_{12}	−0.063	
a_{13}	−0.164	−0.164
a_{23}	0.053	

Table 5
Y_2 coefficients before and after parameter decimation.

Coefficients	Generic Model	Refined Model
b_0	1.113	1.193
b_1	−0.051	
b_2	0.208	0.208
b_3	−0.132	−0.132
b_{11}	0.064	
b_{22}	0.052	
b_{33}	0.005	
b_{12}	−0.065	
b_{13}	0.046	
b_{23}	−0.157	−0.157

points in this 3D space, spheres of varying radius and colour represent estimated response. More details about the 4D mapping procedure can be found in [64]. These 4D maps help visually compare prediction capabilities of GM and RM and confirms that the refining process doesn't alter the capabilities in a significant manner as seen Fig. 4 through the variation of standard deviation.

Based on RM equations *eqs. (10) and (11)*, RM coefficients (Table 4 *and* Table 5) and the expressions of the centred-normalised variables (X_1, X_2, X_3), FT shape ratios ($Y_1 = M_1/M_3$ and $Y_2 = M_1/M_2$) can be expressed as a function of bio-inspired porous pattern parameters $(c/a,\ c/b,\ \rho_f)$ resulting in *eq.(12)*:

$$\begin{cases} \frac{M_1}{M_3} = -0.0069 + 0.9433\ \frac{c}{a} + 1.019\ \rho_f - 0.937\ \frac{c}{a}\ \rho_f \\ \frac{M_1}{M_2} = 0.036 + 0.909\ \frac{c}{b} + 0.968\ \rho_f - 0.897\ \frac{c}{b}\ \rho_f \end{cases} \tag{12}$$

These equations were mapped in 3D space (2 axes for pattern parameters and 1 axis for FT shape ratio) in order to visualise pattern parameters' influence on FT shape ratios. These 3D maps are presented in Fig. 7.

4. 3D mass reduction method inspired from trabecular bone

The mathematical model *eq.(12)* describes the influence of bio-inspired porous pattern parameters on the resulting FT. It can predict FT in the pattern based on the set of parameters. Conversely, it can be used to determine the parameters that produce a target FT and volume fraction in the pattern. Based on this mathematical model, it is possible to mimic the trabecular form-function relationship in a mechanical part. For that purpose, a 3D bio-inspired mass reduction algorithm is established here. This algorithm, detailed in Fig. 8, takes the initial part geometry and loading case as input and outputs a lightweight part geometry.

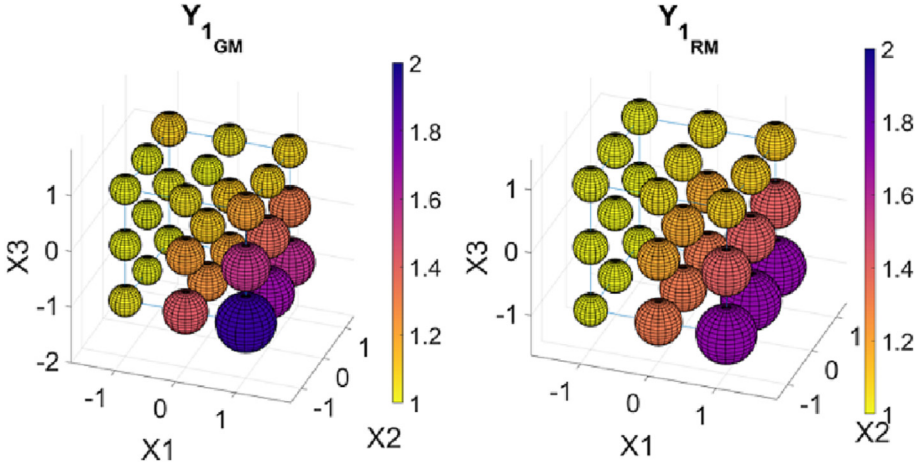

Fig. 5. Y_1 4D response surface comparison between generic model and refined model.

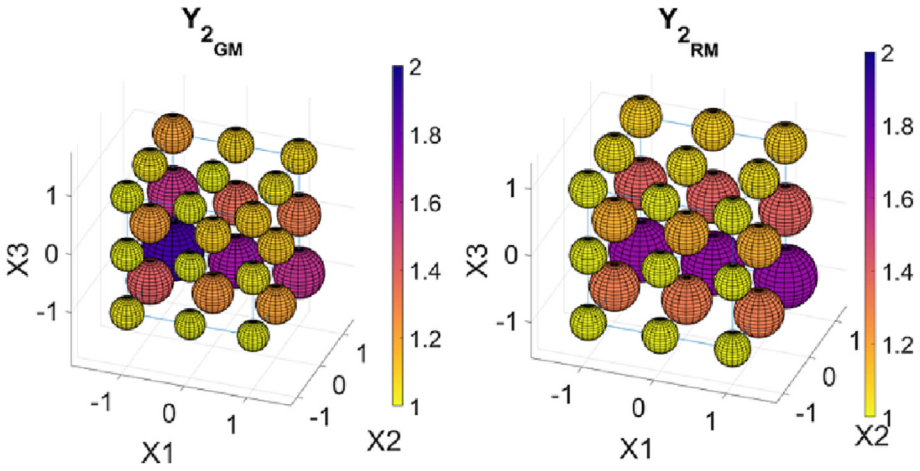

Fig. 6. Y_2 4D response surface comparison between generic model and refined model.

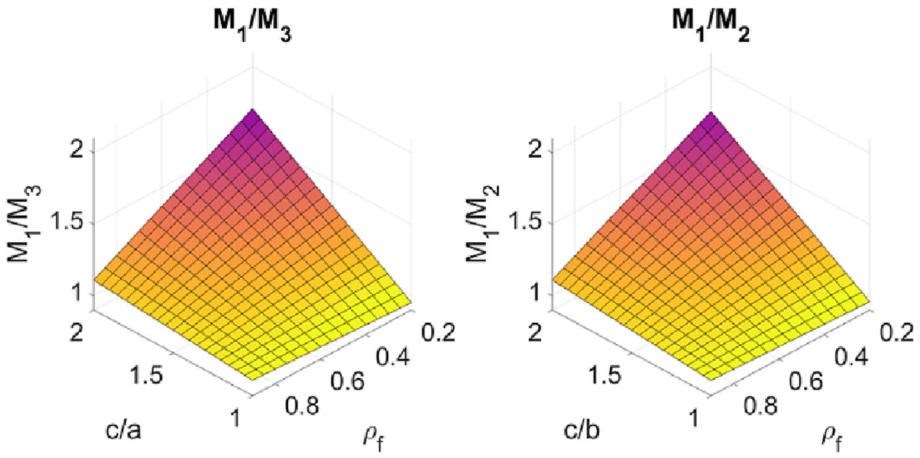

Fig. 7. Y_1 and Y_2 3D response surfaces after parameter decimation.

The initial part geometry is meshed and the local stress tensor at every node is calculated through FEA based on the loading case. This represents the stress field throughout the initial mechanical part. In parallel, nodes are distributed throughout the initial geometry along an FCC pattern of size p. Pattern size p is computed based on the initial part size in a way that mimics trabecular scaling [50]. Both meshes are compared and the corresponding FEA stress tensor is found for every node in the FCC pattern. At each node of the FCC pattern:

- using the sub-algorithm detailed in Fig. 9, both bio-inspired target values for FT and ρ_f are calculated through *eqs.(1) and (3).*
- through *eq.(12),* the pattern parameters necessary to produce the target FT and ρ_f are computed and an ellipsoid porosity is generated.

Note that in the proposed mass reduction method, each porosity will be computed as a function of local stress estimated at the closest FEA node in its vicinity. Hence, in a given FCC unit cells, the porosities will vary in shape, size and orientation. This differs from the geometries used in section 3.2. in which porosities in the FCC unit cell were homogeneous. The fact that individual porosities are positioned at each nodes of the FCC pattern ensures continuity in the overall part.

Through this algorithm, the resulting part mimics the FT and ρ_f gradients that would exist in trabecular bone subjected to the same stress gradient as the initial part. The relevance of the presented 3D bio-inspired mass reduction method was mechanically tested and is presented in the following section.

5. Proof of concept of proposed 3D bio-inspired mass reduction method: 3-point bending case

5.1. Experiment setup

Hence, a 3-point bending case was considered to test the potential of the proposed 3D bio-inspired mass reduction method. 3 designs of equal mass were compared:

- One bio-inspired from mammalian bone in 2D and extruded (BI2.5D) (adapted from [50]);
- One designed using topology optimisation (TO) (adapted from [50]);
- One created with the proposed method (BI3D).

The initial tested beam dimensions are 150 mm × 30 mm × 30 mm. These dimensions were selected based on Audibert *et al.*'s experimental conditions to ease comparison.

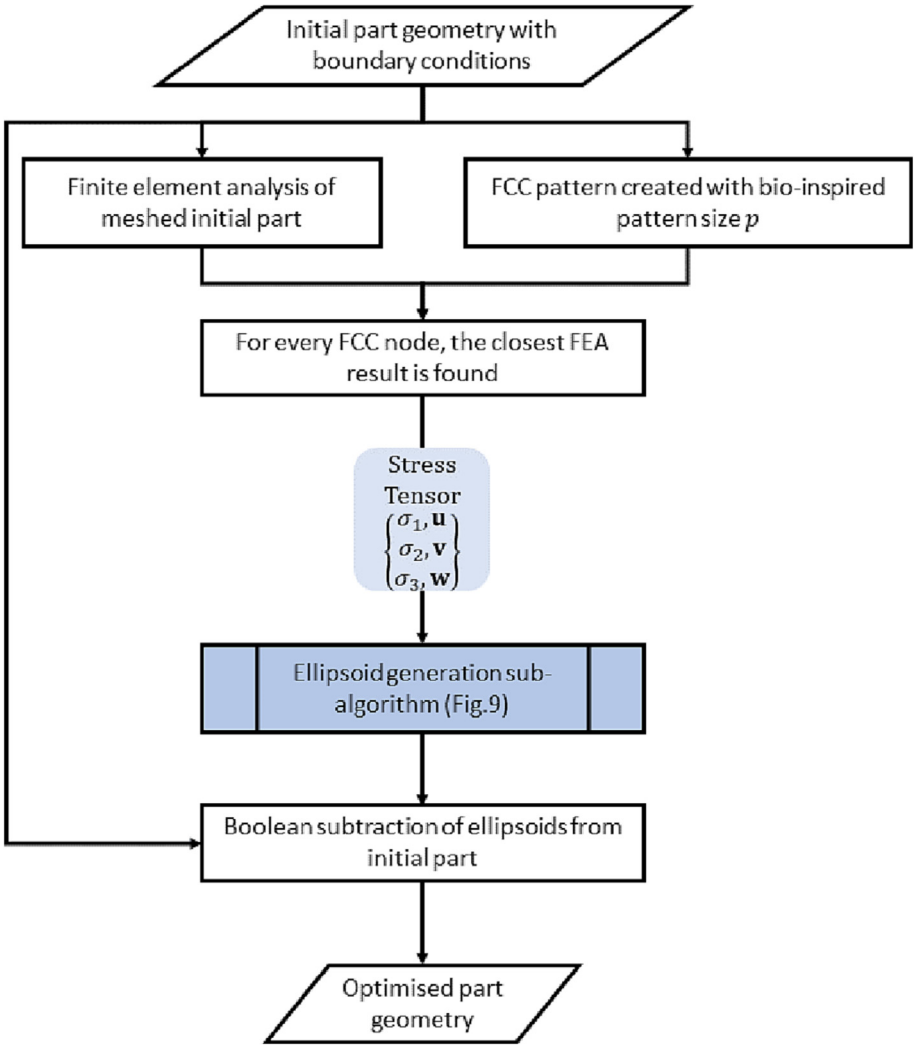

Fig. 8. Mass reduction algorithm.

First, a finite element analysis of the initial 3-point bending beam was conducted using CATIA simulate workbench. The part was meshed with first-order tetrahedral elements of size 2.5 mm. Boundary conditions were applied according to Fig. 10 which illustrates the Von Mises stress found in a solid 3-point bending beam.

BI3D was designed by applying the proposed mass-reduction algorithm to the initial part based on the resulting stress field. Since we seek to compare BI3D to Audibert *et al.*'s samples, the same pattern size $p = 3mm$ was chosen. In their work, the pattern size was calculated based on an equation that reproduces the allometric scaling between trabecular pattern and species size. All 3 designs are shown in Fig. 11. By comparing Fig. 10 *and* Fig. 11, it is possible to see how the local Von Mises stress amplitude in the initial part influences the bio-inspired porous architecture in BI3D. This is a good illustration of how the proposed mass reduction algorithm works.

The beams were manufactured under the same conditions using plastic filament extrusion on a Volumic STREAM 30 Dual Mk.2. Process parameters were:

- Material: Polylactic acid compound (UNIVERSAL ULTRA - PLC)
- Layer thickness: 0.15 mm
- Nozzle temperature: 235 °c
- Tray temperature: 65 °c
- Infill density: 100%

This resulted in 3 beams with respective masses of:

- M_{BI3D} = 106.76 g (theoretical mass based on slicer software Cura: M_{BI3D}=106 g)
- $M_{BI2.5D}$ = 103.29 g (theoretical mass based on slicer software Cura: $M_{BI2.5D}$=103 g)
- M_{TO} = 103.29 g (theoretical mass based on slicer software Cura: M_{TO}=103 g)

5.2. Mechanical testing results

The aforementioned 3 beams were subjected to 3-point bending tests as shown in Fig. 12. During testing, a cylindrical metal pusher applies displacement (δ) on the upper beam face. Beams are supported by metal cylinders spaced 130 mm apart (10 mm from the edges). Plastic 3D printed supports which ensure correct positioning are installed on a multicomponent dynamometer through which vertical force (F_z) is measured. Then, F_z was plotted as a function of δ and measured points were fitted (least square method) to a linear function of form $F_z = A.\delta + B$ with A the slope and B the intercept. A represents the bending stiffness of the tested beam design which was chosen as an indicator of mechanical performance.

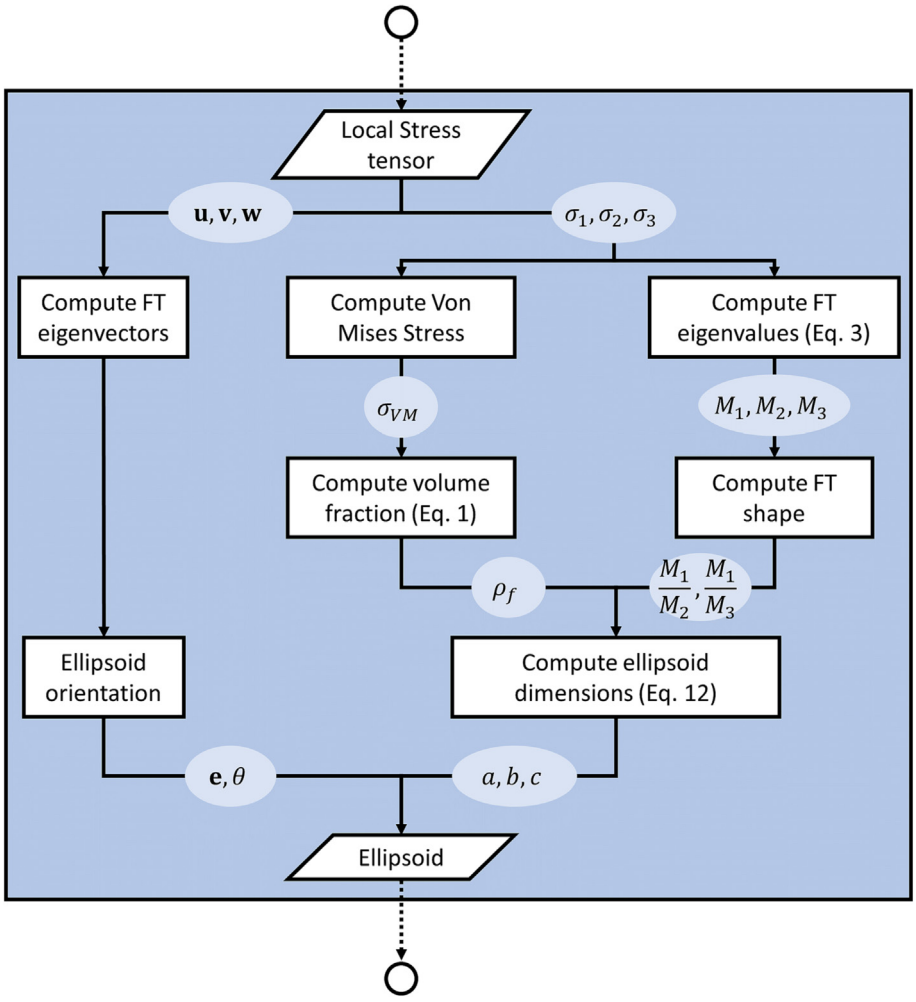

Fig. 9. Ellipsoid generation sub-algorithm.

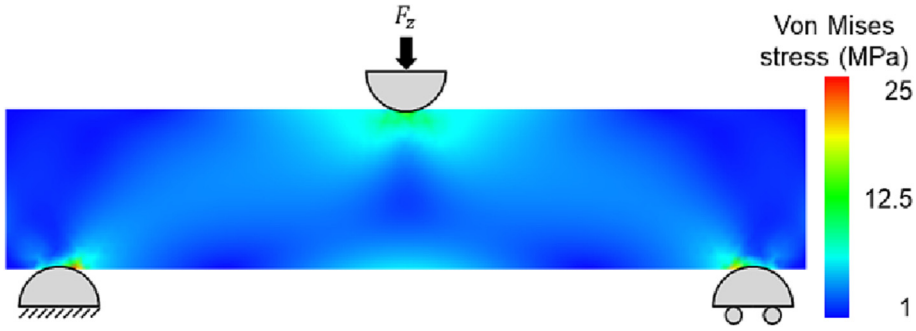

Fig. 10. Von Mises stress field in a solid beam subjected to 3-point bending.

Fig. 13 compares the bending stiffness of the different designs. The 2.5D bio-inspired beam design taken from Audibert *et al.* [50] was taken as reference for comparison. TO shows 21 % decrease in bending stiffness when compared to BI2.5D, which confirms results from [50]. BI3D shows a 66 % increase in bending stiffness when compared to BI2.5D or a 111 % increase when compared to TO (more than twice as stiff).

6. Discussion

In this article, a 3D mass reduction method bio-inspired from the trabecular form-function relationship was presented. Currently, the expression of the trabecular form-function relationship is still being investigated in the biomechanical literature. In particular, it is still debated whether fabric tensor aligns with principal stress directions in trabecular bone [57]. Indeed, during its lifetime, a bone will be subjected to a wide range of loading conditions. Depending on the loading condition, principal stress will vary inside the bone on a short time scale. This could also be due to the complexity of the metabolic phenomenon involved in bone remodelling. Still, Musy *et al.* have shown that variations in trabecular mechanical properties can be explained up to 76% through variations in volume fraction and up to 98% when both volume fraction and fabric tensor are considered [48]. Hence in this article,

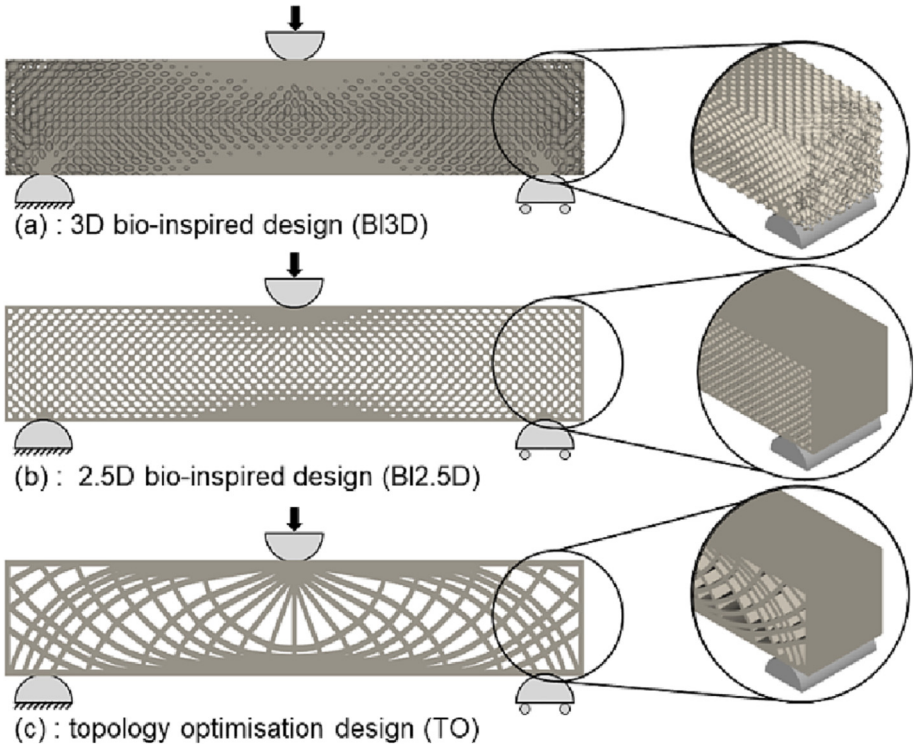

Fig. 11. 3-point bending beam designs.

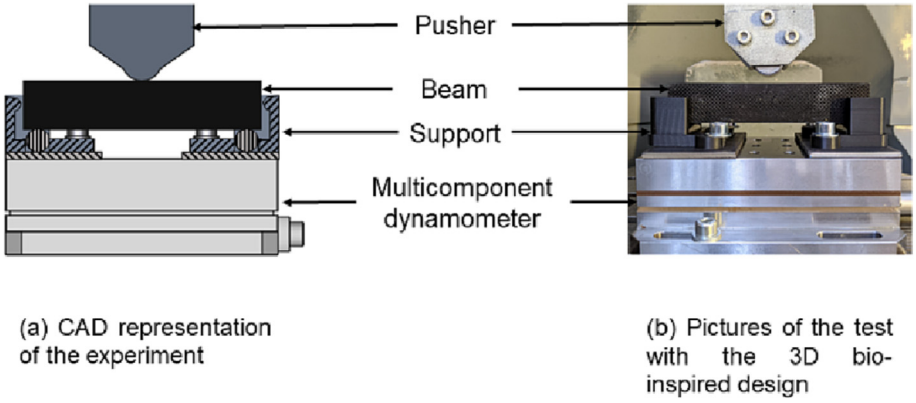

Fig. 12. 3-point bending test.

to reflect the work of several authors [49,57,60], the choice was made to align FT with principal stress. To abstract the complex trabecular form-function relationship, two equations were selected in the literature. These equations link mechanical stress to characteristics of the trabecular architecture: Audibert *et al.* showed that Von Mises stress σ_{VM} could be used to estimate volume fraction [50] and Hazrati Marangalou *et al.* showed that principal stress could be used to estimate fabric tensor [57].

Our results highlight that porosity shape ratio in the bio-inspired porous pattern has a strong influence on FT shape and thus on the anisotropic mechanical behaviour of the material. Indeed, based on *eqs. (10) and (11)* and their respective coefficients in Table 4 *and* Table 5, it is apparent that the first and second FT shape ratios (Y_1, Y_2) in the chosen bio-inspired porous pattern will vary based on the first and second porosity shape ratios (X_1, X_2) respectively. This is expected as the first porosity shape ratio will influence the amount of material in its plane which directly impacts the first FT shape ratio. The second porosity shape ratio doesn't have any significant influence on the first FT shape ratio in the studied data range. On the contrary, the second FT shape ratio is mostly dependant on the second porosity shape ratio; the first porosity shape ratio doesn't have significant influence. The coefficients are positive for both equations which means that the porosity shape directly influence FT shape in the same direction.

The implemented decimation of the model highlights that there's a linear relationship between porosity shape, volume fraction and FT shape. Indeed, based on Fig. 4, coefficients associated with squared variables $(a_{11}, a_{22}, a_{33}, b_{11}, b_{22}, b_{33})$ are the first to be removed when the model is refined. This explains why the first decimation steps don't have much influence on standard deviations and on the prediction capabilities of both models, as illustrated in Fig. 5 and Fig. 6. At first, refining the model transforms the second order polynomials into a linear model which allows precise prediction. Further simplification of the model doesn't take the whole phenomenon into account and is less precise. Hence, the refining was stopped before precision decreased significantly.

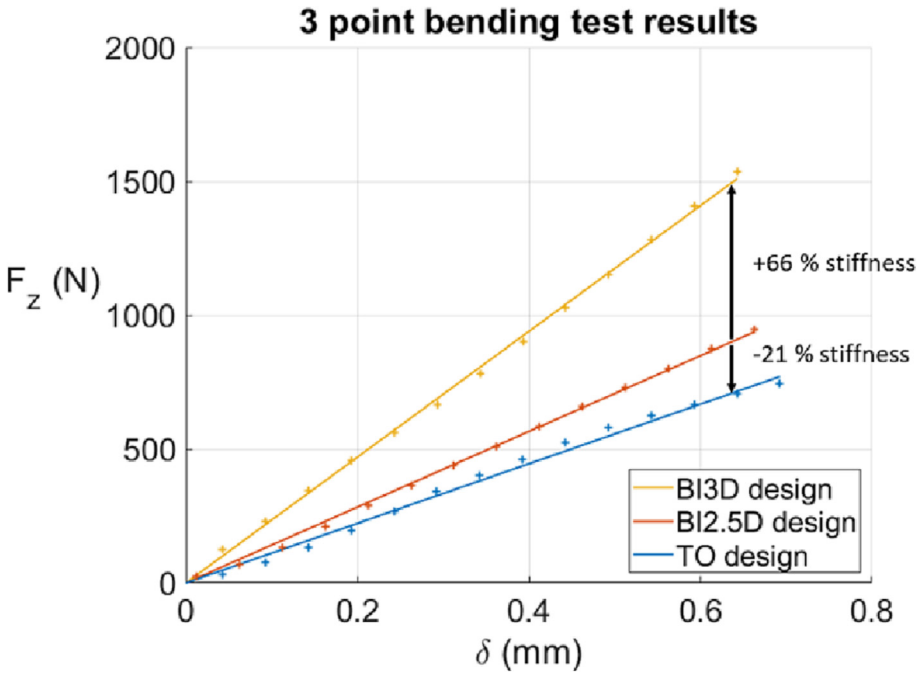

Fig. 13. 3-point bending test results for the different tested beam designs.

Furthermore, results show that volume fraction has an influence on both FT shape ratios, especially for low volume fraction. This is apparent in Fig. 7 which presents the influence of porosity shape and volume fraction on FT shape. For low volume fraction, porosity shape will highly influence the resulting FT shape whereas that's not the case for high volume fraction. This is partly due to the cross coefficient in both equations. Indeed, geometry will change heavily depending on the volume fraction for the same porosity shape. For different patterns with the same porosity shape, the ones with lower volume fraction (less material) will be more anisotropic.

Regarding the geometry of parts optimised with the proposed mass reduction method, Fig. 11 shows that porosities in BI3D are oriented along the principal stress directions in accordance with the algorithm. This is also the case for BI2.5D. Furthermore, no porosities appear in the vicinity of contact zones for both BI2.5D and BI3D. This is consistent with Fig. 10 which shows that these are the most stressed areas. These areas would, in long bones, showcase cortical rather than trabecular bone. On the other hand, areas of low stress are highly porous as can be seen in the detailed views in Fig. 11. The architecture in these areas is very open and resembles trabecular samples such as the ones shown in Fig. 1.

As presented in Fig. 13, all 3 beam designs deform linearly based on applied vertical displacement. This is consistent with the behaviour of a solid beam submitted to 3-point bending which indicates that macrostructure dictates mechanical behaviour. But, despite being of equal mass, all 3 designs have different bending stiffness which confirms that microstructure influences mechanical performance. Compared to TO, a mass reduction method widely used in various industries, both BI2.5D and BI3D show higher bending stiffness. Indeed, both architectures present a network of small porosities which are able to evenly spread mechanical stresses whereas TO presents slender beams which might be subject to buckling. This showcases the potential of bio-inspired mass reduction methods for mechanical design in a variety of industrial sectors. In particular, BI3D showcases a significant increase in bending stiffness compared to BI2.5D and TO. This increase in mechanical behaviour could be explained by the fact that BI3D is a 3-dimensional architecture whereas the other two are extruded 2-dimensional architectures. This hints to the fact that even for planar symmetric loading conditions (3)-point bending) 3D architectures may be relevant for optimisation of mechanical properties.

7. Conclusion

This work sought to establish a 3D mass reduction method that draws inspiration from the trabecular bone form-function relationship.

A bio-inspired porous FCC pattern with ellipsoid porosities was built in order to mimic trabecular bone's volume fraction and Fabric Tensor. A mathematical model was built and refined in order to understand the influence of pattern parameters on the resulting Fabric Tensor. This enables the calculation of pattern parameters which reproduce target volume fraction and Fabric Tensor.

Based on that knowledge, a 3D bio-inspired mass reduction method was proposed. Using the inputted initial part geometry and loading case, it estimates the stress field using FEA, calculates target volume fraction and Fabric Tensor gradients based on trabecular form-function relationship and generates ellipsoid porosities throughout the part. It then outputs the resulting lightweighted part.

The proposed mass reduction method was tested using 3-point bending experiments. Two bending beam designs of equal mass were taken from a previous study. A third design was generated using the proposed mass reduction method in order to achieve the same mass. Based on the results of these experiments, the proposed 3D mass reduction method allows for a 66 % increase in bending stiffness at equal mass when compared to Audibert *et al's* 2.5D method and a 111 % increase when compared to topology optimisation. Hence, the proposed mass reduction method has great potential for mechanical design in a variety of industrial sectors.

The main contributions of this article are:

(i) The complex trabecular form-function relationship was condensed into 2 equations. The first links volume fraction to the Von Mises stress. The second links Fabric Tensor eigenvalues to principal stress.
(ii) A bio-inspired porous pattern was proposed to reproduce the trabecular form-function relationship. This pattern's geometry adapts to stress based on a mathematical model.
(iii) Based on the aforementioned bio-inspired porous pattern, a 3D mass reduction method was established. In this method, size, orientation and shape of elliptical porosities is locally adapted to the state of stress.
(iv) In 3-point bending, the proposed 3D mass reduction method result is more than twice as stiff, at equal mass, when compared to topology optimization.

The proposed method is adequate for statically loaded parts manufactured through material extrusion methods. Nonetheless, for parts loaded dynamically, the fatigue behaviour of the resulting architectures should be investigated. Furthermore, to broaden the scope to powder-bed fusion methods, the architectures should be modified to ensure that all un-melted powders can be removed.

CRediT authorship contribution statement

Nicolas Cadoret: Conceptualization, Data curation, Formal analysis, Investigation, Methodology, Resources, Software, Visualization, Writing – original draft, Writing – review & editing. **Julien Chaves-Jacob:** Conceptualization, Formal analysis, Funding acquisition, Investigation, Methodology, Project administration, Resources, Software, Supervision, Validation, Visualization, Writing – review & editing. **Jean-Marc Linares:** Conceptualization, Formal analysis, Funding acquisition, Investigation, Methodology, Project administration, Supervision, Validation, Visualization, Writing – review & editing.

Data availability

Data will be made available on request.

Declaration of Competing Interest

The authors declare that they have no known competing financial interests or personal relationships that could have appeared to influence the work reported in this paper.

Acknowledgment

The experimental equipment was funded by the European Community, French Ministry of Research and Education and Aix-Marseille Conurbation Community.

References

[1] IPCC 2021: Summary for policymakers, in: Climate Change 2021: The Physical Science Basis. Contribution of Working Group I to the Sixth Assessment Report of the Intergovernmental Panel on Climate Change, Cambridge University Press, 2021.
[2] A. du Plessis, C. Broeckhoven, I. Yadroitsava, I. Yadroitsev, C.H. Hands, R. Kunju, D. Bhate, Beautiful and functional: a review of biomimetic design in additive manufacturing, Additive Manuf. 27 (2019) 408–427, https://doi.org/10.1016/j.addma.2019.03.033.
[3] D. O'Connor, Additive manufacturing for production, Altair (2020). https://www.altair.com/resource/additive-manufacturing-for-production.
[4] B. Blakey-Milner, P. Gradl, G. Snedden, M. Brooks, J. Pitot, E. Lopez, M. Leary, F. Berto, A. du Plessis, Metal additive manufacturing in aerospace: a review, Mater. Design. 209 (2021), https://doi.org/10.1016/j.matdes.2021.110008 110008.
[5] L.R. Meza, S. Das, J.R. Greer, Strong, lightweight, and recoverable three-dimensional ceramic nanolattices, Science 345 (2014) 1322–1326, https://doi.org/10.1126/science.1255908.
[6] M.F. Ashby, Materials selection in mechanical design, Elsevier Science, 2016.
[7] A.M. Torres, A.A. Trikanad, C.A. Aubin, F.M. Lambers, M. Luna, C.M. Rimnac, P. Zavattieri, C.J. Hernandez, Bone-inspired microarchitectures achieve enhanced fatigue life, PNAS. 116 (2019) 24457–24462, https://doi.org/10.1073/pnas.1905814116.
[8] L.J. Gibson, Biomechanics of cellular solids, J. Biomechanics 38 (2005) 377–399, https://doi.org/10.1016/j.jbiomech.2004.09.027.
[9] P. Fratzl, R. Weinkamer, Nature's hierarchical materials, Progress in Mater. Sci. 52 (2007) 1263–1334, https://doi.org/10.1016/j.pmatsci.2007.06.001.
[10] S.E. Naleway, M.M. Porter, J. McKittrick, M.A. Meyers, Structural design elements in biological materials: application to bioinspiration, Adv. Mater. 27 (2015) 5455–5476, https://doi.org/10.1002/adma.201502403.
[11] N. Reznikov, R. Shahar, S. Weiner, Bone hierarchical structure in three dimensions, Acta Biomaterialia. 10 (2014) 3815–3826, https://doi.org/10.1016/j.actbio.2014.05.024.
[12] G. Byrne, D. Dimitrov, L. Monostori, R. Teti, F. van Houten, R. Wertheim, Biologicalisation: biological transformation in manufacturing, CIRP J. Manuf. Sci. Technol. 21 (2018) 1–32, https://doi.org/10.1016/j.cirpj.2018.03.003.
[13] I. Goda, M. Assidi, S. Belouettar, J.F. Ganghoffer, A micropolar anisotropic constitutive model of cancellous bone from discrete homogenization, J. Mechanical Behavior of Biomed. Mater. 16 (2012) 87–108, https://doi.org/10.1016/j.jmbbm.2012.07.012.
[14] I. Goda, R. Rahouadj, J.-F. Ganghoffer, Size dependent static and dynamic behavior of trabecular bone based on micromechanical models of the trabecular architecture, Int. J. Eng. Sci. 72 (2013) 53–77, https://doi.org/10.1016/j.ijengsci.2013.06.013.
[15] S. Burgess, A review of linkage mechanisms in animal joints and related bioinspired designs, Bioinspir. Biomim. 16 (2021), https://doi.org/10.1088/1748-3190/abf744 041001.
[16] R. Oftadeh, M. Perez-Viloria, J.C. Villa-Camacho, A. Vaziri, A. Nazarian, Biomechanics and mechanobiology of trabecular bone: a review, J. Biomechanical Eng. 137 (2015), https://doi.org/10.1115/1.4029176 010802.
[17] H.M. Frost, Bone mass and the mechanostat: a proposal, Anat. Rec. 219 (1987) 1–9, https://doi.org/10.1002/ar.1092190104.
[18] H.M. Frost, Bone's mechanostat: a, update, Anat. Rec. 275A (2003) 1081–1101, https://doi.org/10.1002/ar.a.10119.
[19] J. Park, A. Sutradhar, J.J. Shah, G.H. Paulino, Design of complex bone internal structure using topology optimization with perimeter control, Computers in Biol. Med. 94 (2018) 74–84, https://doi.org/10.1016/j.compbiomed.2018.01.001.
[20] C. Boyle, I.Y. Kim, Three-dimensional micro-level computational study of Wolff's law via trabecular bone remodeling in the human proximal femur using design space topology optimization, J. Biomechanics 44 (2011) 935–942, https://doi.org/10.1016/j.jbiomech.2010.11.029.
[21] M. Huo, S. He, Y. Zhang, Y. Feng, J. Lu, Simulation on bone remodeling with stochastic nature of adult and elderly using topology optimization algorithm, J. Biomechan. 136 (2022), https://doi.org/10.1016/j.jbiomech.2022.111078 111078.
[22] R. Huiskes, H. Weinans, H.J. Grootenboer, M. Dalstra, B. Fudala, T.J. Slooff, Adaptive bone-remodeling theory applied to prosthetic-design analysis, J. Biomechan. 20 (1987) 1135–1150, https://doi.org/10.1016/0021-9290(87)90030-3.
[23] K. Tsubota, T. Adachi, Y. Tomita, Functional adaptation of cancellous bone in human proximal femur predicted by trabecular surface remodeling simulation toward uniform stress state, J. Biomechan. 35 (2002) 1541–1551, https://doi.org/10.1016/S0021-9290(02)00173-2.
[24] K. Tsubota, Y. Suzuki, T. Yamada, M. Hojo, A. Makinouchi, T. Adachi, Computer simulation of trabecular remodeling in human proximal femur using large-scale voxel FE models: approach to understanding Wolff's law, J. Biomechan. 42 (2009) 1088–1094, https://doi.org/10.1016/j.jbiomech.2009.02.030.
[25] I. Goda, J.-F. Ganghoffer, G. Maurice, Combined bone internal and external remodeling based on Eshelby stress, Int. J. Solids and Struct.. 94–95 (2016) 138–157, https://doi.org/10.1016/j.ijsolstr.2016.04.036.
[26] I. Goda, J.-F. Ganghoffer, S. Czarnecki, P. Wawruch, T. Lewiński, Optimal internal architectures of femoral bone based on relaxation by homogenization and isotropic material design, Mechan. Res. Commun. 76 (2016) 64–71, https://doi.org/10.1016/j.mechrescom.2016.06.007.
[27] C. Pan, Y. Han, J. Lu, Design and optimization of lattice structures: a review, Appl. Sciences 10 (2020) 6374, https://doi.org/10.3390/app10186374.
[28] X. Wang, L. Zhu, L. Sun, N. Li, Optimization of graded filleted lattice structures subject to yield and buckling constraints, Mater.& Design 206 (2021), https://doi.org/10.1016/j.matdes.2021.109746 109746.
[29] A.L. Ruschel, A.F. Samuel, M.C. Martinez, M.R. Begley, F.W. Zok, A 3D bi-material lattice concept for tailoring compressive properties, Mater. & Design. 224 (2022), https://doi.org/10.1016/j.matdes.2022.111265 111265.
[30] H.-Y. Lei, J.-R. Li, Z.-J. Xu, Q.-H. Wang, Parametric design of Voronoi-based lattice porous structures, Mater. & Design 191 (2020), https://doi.org/10.1016/j.matdes.2020.108607 108607.
[31] J. Deering, K.I. Dowling, L.-A. DiCecco, G.D. McLean, B. Yu, K. Grandfield, Selective Voronoi tessellation as a method to design anisotropic and biomimetic implants, J. Mechan. Behavior of Biomed. Mater. 116 (2021), https://doi.org/10.1016/j.jmbbm.2021.104361 104361.

[32] M. Fantini, M. Curto, F. De Crescenzio, A method to design biomimetic scaffolds for bone tissue engineering based on Voronoi lattices, Virtual and Phys. Prototyping 11 (2016) 77–90, https://doi.org/10.1080/17452759.2016.1172301.
[33] M. Fantini, M. Curto, Interactive design and manufacturing of a Voronoi-based biomimetic bone scaffold for morphological characterization, Int. J. Interact Des. Manuf. 12 (2018) 585–596, https://doi.org/10.1007/s12008-017-0416-x.
[34] J. Li, D. Guo, J. Li, X. Wei, Z. Sun, B. Yang, T. Lu, P. Ouyang, S. Chang, W. Liu, X. He, Irregular pore size of degradable bioceramic Voronoi scaffolds prepared by stereolithography: osteogenesis and computational fluid dynamics analysis, Mater. Design. 224 (2022), https://doi.org/10.1016/j.matdes.2022.111414 111414.
[35] A. Viswanath, K.A. Khan, I. Barsoum, Design of novel isosurface strut-based lattice structures: effective stiffness, strength, anisotropy and fatigue properties, Mater. & Design 224 (2022), https://doi.org/10.1016/j.matdes.2022.111293 111293.
[36] J. Shi, L. Zhu, L. Li, Z. Li, J. Yang, X. Wang, A TPMS-based method for modeling porous scaffolds for bionic bone tissue engineering, Sci. Rep. 8 (2018) 7395, https://doi.org/10.1038/s41598-018-25750-9.
[37] D. Li, N. Dai, Y. Tang, G. Dong, Y.F. Zhao, Design and optimization of graded cellular structures with triply periodic level surface-based topological shapes, J. Mechanical Design 141 (2019), https://doi.org/10.1115/1.4042617.
[38] D.W. Abueidda, M. Elhebeary, C.-S. (Andrew) Shiang, S. Pang, R.K. Abu Al-Rub, I.M. Jasiuk, Mechanical properties of 3D printed polymeric Gyroid cellular structures: experimental and finite element study, Mater. & Design. 165 (2019), https://doi.org/10.1016/j.matdes.2019.107597 107597.
[39] D. Li, W. Liao, N. Dai, Y.M. Xie, Anisotropic design and optimization of conformal gradient lattice structures, Comput.-Aided Design 119 (2020), https://doi.org/10.1016/j.cad.2019.102787 102787.
[40] X. Zhang, L. Jiang, X. Yan, Z. Wang, X. Li, G. Fang, Regulated multi-scale mechanical performance of functionally graded lattice materials based on multiple bioinspired patterns, Mater. & Design 226 (2023), https://doi.org/10.1016/j.matdes.2022.111564 111564.
[41] L. Xu, N. Hoffman, Z. Wang, H. Xu, Harnessing structural stochasticity in the computational discovery and design of microstructures, Mater. & Design 223 (2022), https://doi.org/10.1016/j.matdes.2022.111223 111223.
[42] S. Kumar, S. Tan, L. Zheng, D.M. Kochmann, Inverse-designed spinodoid metamaterials, Npj Comput. Mater. 6 (2020) 1–10, https://doi.org/10.1038/s41524-020-0341-6.
[43] ISO 18458:2015 Biomimetics - Terminology, concepts and methodology, (2015). https://www.iso.org/standard/62500.html.
[44] J. Wolff, The law of bone remodelling, Springer Science & Business Media, 2012.
[45] J. Wolff, The Classic: on the Inner Architecture of Bones and its Importance for Bone Growth: (Ueber die innere Architectur der Knochen und ihre Bedeutung für die Frage vom Knochenwachsthum), Clin. Orthopaedics and Related Res.®. 468 (2010) 1056–1065, https://doi.org/10.1007/s11999-010-1239-2.
[46] R. Huiskes, If bone is the answer, then what is the question?, J Anatomy. 197 (2000) 145–156, https://doi.org/10.1046/j.1469-7580.2000.19720145.x.
[47] M. Doube, M.M. Kłosowski, A.M. Wiktorowicz-Conroy, J.R. Hutchinson, S.J. Shefelbine, Trabecular bone scales allometrically in mammals and birds, Proc. R. Soc. B. 278 (2011) 3067–3073, https://doi.org/10.1098/rspb.2011.0069.
[48] S.N. Musy, G. Maquer, J. Panyasantisuk, J. Wandel, P.K. Zysset, Not only stiffness, but also yield strength of the trabecular structure determined by non-linear μFE is best predicted by bone volume fraction and fabric tensor, J. Mechanical Behavior of Biomed. Mater. 65 (2017) 808–813, https://doi.org/10.1016/j.jmbbm.2016.10.004.
[49] C.H. Turner, On Wolff's law of trabecular architecture, J. Biomechan. 25 (1992) 1–9, https://doi.org/10.1016/0021-9290(92)90240-2.
[50] C. Audibert, J. Chaves-Jacob, J.-M. Linares, Q.-A. Lopez, Bio-inspired method based on bone architecture to optimize the structure of mechanical workspieces, Mater. Design 160 (2018) 708–717, https://doi.org/10.1016/j.matdes.2018.10.013.
[51] M. Bilhère-Dieuzeide, J. Chaves-Jacob, E. Buhon, G. Biguet-Mermet, J.-M. Linares, Stress-driven method bio-inspired by long bone structure for mechanical part mass reduction by removing geometry at macro and cell-unit scales, Mater. & Design. 213 (2022), https://doi.org/10.1016/j.matdes.2021.110318 110318.
[52] S.C. Cowin, The relationship between the elasticity tensor and the fabric tensor, Mechanics of Mater. 4 (1985) 137–147, https://doi.org/10.1016/0167-6636(85)90012-2.
[53] W.J. Whitehouse, The quantitative morphology of anisotropic trabecular bone, J. Microscopy 101 (1974) 153–168, https://doi.org/10.1111/j.1365-2818.1974.tb03878.x.
[54] T.P. Harrigan, R.W. Mann, Characterization of microstructural anisotropy in orthotropic materials using a second rank tensor, J. Mater. Sci. 19 (1984) 761–767, https://doi.org/10.1007/BF00540446.
[55] M. Doube, M.M. Kłosowski, A.M. Wiktorowicz-Conroy, J.R. Hutchinson, S.J. Shefelbine, Trabecular bone scales allometrically in mammals and birds - Electronic Supplementary Mater. (2011), https://doi.org/10.1098/rspb.2011.0069.
[56] R. Domander, A.A. Felder, M. Doube, BoneJ2 - refactoring established research software, Wellcome Open Res. 6 (2021) 37. https://doi.org/10.12688/wellcomeopenres.16619.1.
[57] J. Hazrati Marangalou, K. Ito, B. van Rietbergen, A novel approach to estimate trabecular bone anisotropy from stress tensors, Biomech Model Mechanobiol. 14 (2015) 39–48, https://doi.org/10.1007/s10237-014-0584-6.
[58] N. Cadoret, J. Chaves-Jacob, J.-M. Linares, A. Houssaye, Form-function relationship between trabecular bone architecture and biomechanical function in the horse humerus, in: Procedia CIRP, 2022: pp. 299–304. https://doi.org/10.1016/j.procir.2022.06.054.
[59] FreeCAD, (2022). https://github.com/FreeCAD/FreeCAD (accessed January 18, 2022).
[60] P.K. Zysset, R.W. Goulet, S.J. Hollister, A global relationship between trabecular bone morphology and homogenized elastic properties, J. Biomechanical Eng. 120 (1998) 640–646, https://doi.org/10.1115/1.2834756.
[61] S.D. Brown, R. Tauler, B. Walczak, Comprehensive chemometrics: chemical and biochemical data analysis, Elsevier, 2020.
[62] G.A. Lewis, D. Mathieu, R. Phan-Tan-Luu, Pharmaceutical experimental design, CRC Press, 1998.
[63] P. Courrieu, Fast Computation of Moore-Penrose Inverse Matrices, (2008). http://arxiv.org/abs/0804.4809 (accessed July 16, 2021).
[64] M. Moumen, J. Chaves-Jacob, M. Bouaziz, J.-M. Linares, Optimization of pre-polishing parameters on a 5-axis milling machine, Int. J. Adv. Manuf. Technol. 85 (2016) 443–454, https://doi.org/10.1007/s00170-015-7944-y.